Hyperfine measurements of the $^1D_2$-$^3H_4$ transition in Pr^{3+}: Yttrium aluminum garnet using photon echo

M. K. Kim
Department of Physics and Astronomy, Wayne State University, Detroit, Michigan 48202

R. Kachru
Molecular Physics Laboratory, SRI International, Menlo Park, California 94025
(Received 8 February 1989)

The hyperfine structure of the $^1D_2$-$^3H_4$ transition of Pr^{3+}: yttrium aluminum garnet (YAG) is studied using a photon echo modulation technique. The Fourier transform of modulation data gives hyperfine frequencies of the $^1D_2$ state as 3.42 and 5.96 MHz. The photon echo modulation is a very sensitive function of the atomic environment, and we find that the site symmetry of Pr^{3+} impurity ions in YAG is lowered to C_2 from the D_2 symmetry of Y^{3+} ions.

I. INTRODUCTION

Considerable attention has been given recently to the study of hyperfine interaction and relaxation of the excited states of Pr^{3+} ions in single crystals. In particular, the hyperfine interaction of the $^3H_4$ ground and $^1D_2$ and $^3P_0$ excited states of Pr^{3+} doped in LaF_3 has been investigated, as has been the homogeneous relaxation time T_2 of the transitions.[1-14] In this work, we report the investigation of the hyperfine interaction Hamiltonian of $^3H_4$ and $^1D_2$ states of Pr^{3+} in the popular laser material yttrium aluminum garnet (YAG) using photon echo modulation, for which there have been relatively few studies reported.[15] The interference of hyperfine levels excited by the broadband laser modulates the rephasing of the photon echo signal. This modulation reveals the hyperfine frequencies, orientation, and linewidths.

The photon echo modulation technique[1,5,7,8,10,16-18] has been fruitfully used to study hyperfine interaction of impurity ions in solids. Just as two examples, Lambert[16] studied superhyperfine interaction of Cr-Al ions in ruby and Pr^{3+}:LaF_3 has been thoroughly investigated by a number of groups including Chen, *et al.*[1,5,7,10] As with many other optical transient phenomena, the NMR analog is found in spin-echo modulation.[19-23] Here the word modulation refers to the variation of the echo signal intensity as a function of the delay time of the excitation pulses. There is also another related but distinct class of echo interference effect, where the envelope of the echo signal itself contains beat structure.[24-26] The physical distinction of these two modulation effects is that in the former case the phase or population memory of the atomic system is periodically modulated by hyperfine interaction for example, whereas in the latter case there is more than one nearly degenerate transition participating in the photon echo formation more or less independently. This corresponds to an echo of quantum-beat free induction decay (FID).[27] Stimulated photon echo can also exhibit modulation.[7,8,18,28] The theory of spin or photon echo and their modulation has been considered by several authors.[10,13,16,18,21,23,25,29] Various double-resonance techniques have proven to be powerful probes of hyperfine structures. These include electron-nuclear double resonance (ENDOR),[30] photon-echo–nuclear double resonance (PENDOR),[11,31-33] and optically detected nuclear quadrupole resonance (ODNQR).[3,34] Hyperfine structures are also revealed in a quantum beat of fluorescence[27] or FID,[2,6] saturated (hole) or enhanced (antihole) absorption[4,12,34] and periodic impact excitation resonance.[35,36] In the last case, one observes narrow resonance of periodic pulse excitation whenever the laser pulse repetition rate or a higher harmonic coincides with the frequency splitting of the coherently excited levels. Raman heterodyne detection of NMR (Ref. 37) has been used to accurately determine nuclear orientation.

We begin in Sec. II with a brief review of the theory of photon-echo modulation for a system with hyperfine structure. The experimental apparatus is described in Sec. III, and the experimental results in Sec. IV. Using the theoretical results of Sec. II, the data is analyzed and compared to the simulation of photon echo modulation in Sec. V to determine the hyperfine parameters.

II. THEORY

In this section we review the theory of photon echo modulation, to be used later in the numerical simulation and compared to experimental data to determine the hyperfine parameters. We follow the density matrix formalism as in Chen *et al.*[10] and Grischkowsky *et al.*,[23] giving only the main results with some clarification. The theory is quite similar in appearance to the case of photon echo in a simple two-level system,[38] except that the ground and excited states contain hyperfine structures. We begin by writing down the Hamiltonian of the system and consider the evolution of the density matrix through interaction between the atoms and laser pulses. Since the laser linewidth is large compared to the hyperfine splittings, the photon-echo signal contains all the components involving different hyperfine levels in the ground and the

excited states, and the beating of these components gives rise to the modulation of the macroscopic signal.

The total Hamiltonian of the atom interacting with the laser is written as

$$H=H_0+H_I+H_R \ , \tag{1}$$

where H_0 represents the energy $\hbar\omega_0$ of the optical transition between the ground state $|g\rangle$ and the excited state $|e\rangle$; H_I is the hyperfine interaction term; and H_R accounts for the interaction with the laser. If we write the laser electric field as

$$\mathbf{E}=\hat{\mathbf{n}}\tfrac{1}{2}(\epsilon e^{i(\mathbf{k}\cdot\mathbf{r}-\omega t)}+\epsilon^* e^{i(\mathbf{k}\cdot\mathbf{r}-\omega t)}) \ , \tag{2}$$

then the total Hamiltonian has the form

$$H=\begin{bmatrix} H_g & -p^*E \\ -pE & \hbar\omega_0+H_e \end{bmatrix} , \tag{3}$$

where $p=\hat{\mathbf{n}}\cdot\mathbf{P}$ is the transition dipole movement and H_g and H_e are the hyperfine interactions in the ground and the excited states, respectively. Therefore, for a nuclear spin I, the total Hamiltonian is a 2×2 block matrix of $(2I+1)\times(2I+1)$ submatrices.

The ^{141}Pr nucleus, the only natural isotope, has spin $I=\frac{5}{2}$ and the hyperfine interaction contains two components: one is the interaction between the electric quadrupole moment of the nucleus and the gradient of the crystal electric field; the other is the second-order hyperfine interaction between the magnetic moment of the nuclear spin and the magnetic field produced by the electrons of the ion. The latter is called the pseudoquadrupole interaction because its Hamiltonian has the same form as the electric quadrupole interaction. Note that for the lowest Stark levels of the ground and excited states, the average electronic angular momentum is zero and the first-order hyperfine interaction $\mathbf{I}\cdot\mathbf{J}$ vanishes. Thus the hyperfine Hamiltonian can be written as, in the respective principal axes systems of ground and excited states,

$$\begin{aligned} H_g&=P_g[I_z^2+\tfrac{1}{3}\eta_g(I_x^2-I_y^2)] \ , \\ H_e&=P_e[I_Z^2+\tfrac{1}{3}\eta_e(I_X^2-I_Y^2)] \ . \end{aligned} \tag{4}$$

The principal axes systems (x,y,z) and (X,Y,Z) are determined by the crystal electric field and electronic charge distribution, and therefore are dependent on the electronic state and constrained by the symmetry of the ionic site. This point will be discussed in Sec. V to determine the relative orientation of the two coordinate systems. Since the hyperfine Hamiltonian is quadratic in the I's, the $(2I+1)$-fold degeneracy is partially lifted, for half-integral spin I, into a series of doublets with $\pm m_I$. Therefore, for the Pr^{3+} ions, there are three doubly degenerate hyperfine levels with $m_I=\pm\frac{5}{2}$, $\pm\frac{3}{2}$, and $\pm\frac{1}{2}$.

In the rotating-reference-frame approximation of ignoring rapidly varying terms at $2\omega t$ compared to static terms, the evolution of the density matrix is given by

$$\frac{d\rho}{dt}=-\frac{i}{\hbar}(H_\omega,\rho) \ , \tag{5}$$

where

$$H_\omega=\begin{bmatrix} H_g & a^* \\ a & H_e+\hbar\Delta \end{bmatrix} \tag{6}$$

and

$$\begin{aligned} a&=-\tfrac{1}{2}p\epsilon e^{i\mathbf{k}\cdot\mathbf{r}} \ , \\ \Delta&=\omega_0-\omega \ . \end{aligned} \tag{7}$$

The area of a laser pulse of length τ_i is defined as

$$\Theta_i=\frac{2|a_i|\tau_i}{\hbar}=\frac{|p\epsilon_i|\tau_i}{\hbar} \ . \tag{8}$$

In a photon-echo experiment we apply two laser pulses of areas Θ_1 and Θ_2 separated in time by τ. At time t after the second pulse, the density matrix element ρ_{ge} that contributes to the photon-echo (PE) formation is then given by

$$\begin{aligned} \rho_{ge}(\mathrm{PE})=&-\frac{1}{2I+1}i\sin\left[\frac{\Theta_1}{2}\right]\cos\left[\frac{\Theta_1}{2}\right]\sin^2\left[\frac{\Theta_2}{2}\right]\frac{a_1a_2^{*2}}{|a_1||a_2|^2} \\ &\times\exp\left[-\frac{i}{\hbar}H_gt\right]\exp\left[-\frac{i}{\hbar}(H_e+\hbar\Delta)\tau\right]\exp\left[\frac{i}{\hbar}H_g\tau\right]\exp\left[\frac{i}{\hbar}(H_e+\hbar\Delta)t\right] \end{aligned} \tag{9}$$

which depends on both the first and the second laser pulses (a_1 and a_2) and rephases at $t=\tau$ to yield the photon echo. The photon-echo polarization is then given by

$$P(\mathrm{PE})=2\mathrm{Re}\,\mathrm{Tr}[p\rho_{ge}(\mathrm{PE})]=P_0S \ , \tag{10}$$

where

$$P_0=\mathrm{Re}\left[i\sin\Theta_1\sin^2\left[\frac{\Theta_2}{2}\right]|p|\frac{\epsilon_1\epsilon_2^{*2}}{|\epsilon_1||\epsilon_2|^2}e^{i(\mathbf{k}_1-2\mathbf{k}_2)\cdot\mathbf{r}}e^{i\omega\tau}\right] , \tag{11}$$

$$S=\frac{1}{2I+1}\mathrm{Tr}\left[\exp\left[-\frac{i}{\hbar}H_g\tau\right]\exp\left[-\frac{i}{\hbar}(H_e+\hbar\Delta)\tau\right]\exp\left[\frac{i}{\hbar}H_g\tau\right]\exp\left[\hbar(H_e+\hbar\Delta)\tau\right]\right] \ . \tag{12}$$

From Eq. (11) it follows that the photon echo is maximum for $\Theta_1=\pi/2$ and $\Theta_2=\pi$ and that the echo is emitted in the

direction $\mathbf{k}_e=-\mathbf{k}_1+2\mathbf{k}_2$. The time dependence $e^{i\omega\tau}$ is recovered when we go back to the lab frame. The trace S is evaluated by diagonalizing the hyperfine Hamiltonians H_g and H_e:

$$H_G=U_gH_gU_g^{-1}\ ,$$
$$H_E=U_eH_eU_e^{-1}\ , \tag{13}$$

and defining

$$W=U_eU_g^{-1}\ , \tag{14}$$

$$\omega_{\alpha\gamma}^{(e)}=\frac{i}{\hbar}(H_{E,\alpha\alpha}-H_{E,\gamma\gamma})\ ,$$
$$\omega_{\beta\delta}^{(g)}=\frac{i}{\hbar}(H_{G,\beta\beta}-H_{G,\delta\delta})\ . \tag{15}$$

Then

$$S=\frac{1}{2I+1}\sum_{\alpha,\beta,\gamma,\delta=1}^{2I+1}W_{\alpha\beta}W_{\beta\gamma}^{-1}W_{\gamma\delta}W_{\delta\alpha}^{-1}\cos[(\omega_{\alpha\gamma}^{(e)}-\omega_{\beta\delta}^{(g)})\tau]\exp[-(\Gamma_{\alpha\gamma}^{(e)}+\Gamma_{\beta\delta}^{(g)}+\Gamma)2\tau]\ , \tag{16}$$

which is real and independent of the detuning factor Δ. The photon echo removes the effect of optical inhomogeneous broadening. In addition, we have also included the damping factor that accounts for the decay of modulation due to inhomogeneous broadening, $\Gamma_{\alpha\gamma}^{(e)}$ and $\Gamma_{\beta\delta}^{(g)}$, of the hyperfine levels as well as the overall optical dephasing term Γ. This last expression is the main result of this section and will be used in the numerical simulation in Sec. V.

III. APPARATUS

Figure 1 shows the schematic of the apparatus for measuring photon-echo intensity as a function of the laser pulse delay time. The overall system may be grouped into three parts: various optical components to steer the laser beams and echo signal into and out of the sample crystal; electronics for signal detection and timing pulse generation; and the computer and interfaces for timing control and data acquisition. The second harmonic output of the two Quantaray DCR-1 YAG lasers pump the two pulsed dye lasers, one of which is the Quantaray PDL-1 and the other a homemade Hänsch-type dye laser. The dye laser output is typically 5 nsec, 0.5 mJ pulses of 15 GHz width. The combined beam from these lasers is focused onto the sample to about 10 μm spot by a 30 cm lens. For accurate initial beam alignment, we use a focusing lens-pinhole-collimating lens arrangement on either side of the sample. The 13 mm long Pr^{3+}:YAG crystal, purchased from Crystal Optics Research, is immersed in the liquid-helium cryostat at temperatures down to 1.4 K. The doping concentration of the crystal is not exactly known but is on the order of 0.01% as inferred from absorption measurements. The laser beam out of the sample, along with the photon-echo pulse, is collimated by another lens and passes through the Pockels shutter arrangement, which consists of two stages of crossed Glan prism polarizers with the Pockels cells in between. This allows passage of photon-echo signal with little attenuation while preventing saturation of the photomultiplier with strong input laser pulses. The photon echo signal is detected by an RCA C31034A photomultiplier tube. A narrow-band interference filter at the entrance of the tube housing cuts down stray light.

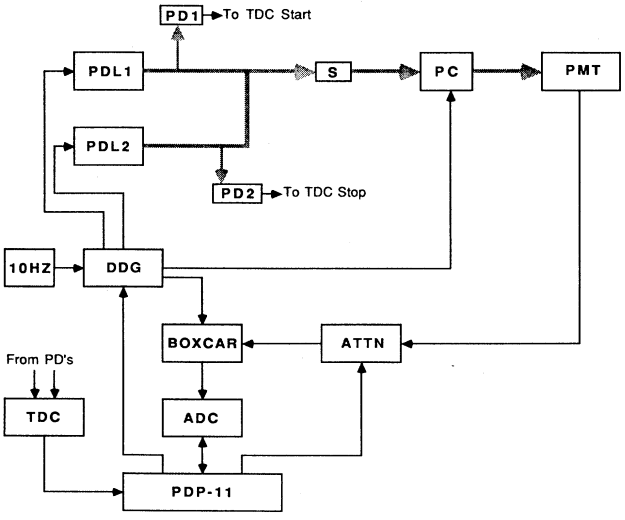

FIG. 1. Schematic of apparatus for photon-echo modulation experiment. PDL's: YAG-pumped pulsed dye lasers. PD's: photodiodes. S: sample crystal of Pr^{3+}:YAG immersed in liquid helium cryostat. PC: Pockels-cell shutter. PMT: photomultiplier tube. 10 HZ: master clock. DDG: digital delay generator. BOXCAR: boxcar gated integrator. ATTN: programmable rf attenuator. ADC: analog-to-digital converter. TDC: time-to-digital converter. PDP-11: microcomputer.

The master timing of the experiment is provided by the 10-Hz clock, that triggers the programmable digital delay generator (SRS DG535), which in turn supplies timing signals to the externally triggered YAG lasers, the Pockels cell trigger unit, the boxcar gate (SRS SR250), and the analog-to-digital converter's external trigger (DEC ADV11C). The actual delay time of the two laser pulses is accurately measured in real time by picking off 5% of the laser beams onto the photodiodes and sending the signal to the time-to-digital converter (LeCroy TDC 4201). To enhance the dynamic range of the measured signal intensity, a preamp and a programmable attenuator is in-

serted between the phototube and the boxcar.

The experiment is under control of the Digital Equipment Corporation PDP-11 microcomputer by programming the digital delay generator and reading the TDC and ADC output. The computer program thus measures the echo intensity, averages the signal, scans the laser delay time, and outputs the data to a graphics terminal and disk files. Another program is used for performing fast Fourier transform of the temporal data into frequency spectra. Details of the experimental procedures are given in the next section.

IV. EXPERIMENT

The lasers are tuned at 6096 Å, corresponding to the transition between the lowest Stark levels of the $^1D_2$ and $^3H_4$ electronic states of Pr^{3+} ions in YAG, whose inhomogeneous width is determined from absorption measurements as about 1.7 cm^{-1}. At the cryostat temperature of 1.4 K, the population is initially all in the lowest Stark level of the ground state $^3H_4$, the nearest Stark level being 17 cm^{-1} away. The two lasers produce pulses at times $t=0$ and $t=\tau$, and the photon echo is emitted from the sample at $t=2\tau$. At each delay time τ, the echo signal is accumulated for 50 shots, and the delay time τ is then scanned from 100 nsec to a few μsec in steps of 5 nsec. The pulse areas are optimized for maximum echo signal using neutral density filters in the paths of the input laser beams. Since the echo intensity can vary by a few orders of magnitude, the programmable attenuator is required to cover the dynamic range of the detected signal. In order to minimize the error due to any optical or electronic interference, the boxcar averager timing is arranged so that two gates are positioned for each cycle, one on top of the echo signal and the other away from it, and the computer takes the difference between the two signals from the boxcar as the net echo signal.

Figure 2 shows two such scans of photon echo intensity as a function of the pulse delay time τ, (a) for τ from 0.1 to 10.0 μsec and (b) from 0.1 to 2.4 μsec, showing the details of the modulation pattern. The simulation results of the next section are also shown in Fig. 2 for convenience of comparison. From Fig. 2(a), where the photon-echo intensity changes by four orders of magnitude, the overall exponential decay time is $\tau=1.3$ μsec, giving the optical dephasing time $T_2=5.2$ μsec. Here a factor of 2 arises because the echo occurs at 2τ, and another factor of 2 is needed because the detector measures the intensity rather than the amplitude of the echo. The optical homogeneous width of the transition is therefore

$$\Gamma=(\pi T_2)^{-1}=61.0 \text{ kHz} .$$

On top of this exponential decay is superimposed the modulation pattern due to beating of the hyperfine frequencies of the ground and the excited states of the transition. The low-frequency components in this pattern at periods of 0.3 μsec or so are from the hyperfine splittings of the $^1D_2$, and lasts more than 10 μsec. The higher frequency components with periods shorter than 30 nsec and lasting only less than 1 μsec are due to the hyperfine splittings in the $^3H_4$ ground state. We also note that in Fig. 2(a) there is a very slow and weak modulation of the decay envelope, at a period of about 6 μsec. This feature has also been observed in the photon echo experiments of another transition $^3P_0$-$^3H_4$ in Pr^{3+}:YAG, which otherwise shows no modulation.[28]

In order to determine the hyperfine frequencies and linewidths accurately from modulation data, fast Fourier

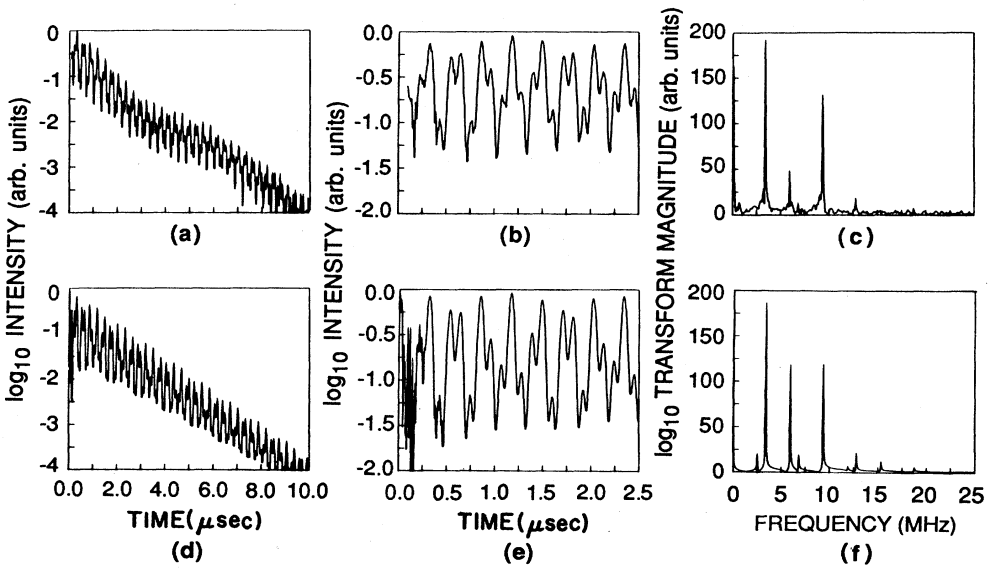

FIG. 2. Photon-echo modulation experimental data, top three figures, and theoretical simulation, bottom three figures. The spectra (c) and (f) are Fourier transforms of (a) and (d), respectively. The parameters used in the simulation are: hf frequencies =3.42, 5.96, and 9.38 MHz for the excited state, and 33.4, 41.6, and 75.0 MHz for the ground state; relative nuclear orientation is $\mathbf{z}\|\mathbf{X}$ and $\angle(x,Y)=30°$, hyperfine inhomogenous linewidths = 2.2 MHz for $^3H_4$ and 20 kHz for $^1D_2$; and optical homogenous width = 61.0 kHz.

transform is performed on it. Before the actual transform, though, the data is divided by the overall exponential decay factor to simplify the interpretation of the linewidths. Also, since the fast Fourier transform algorithm requires 2^N data points, where N is an integer, we simply pad zeroes at the end of the data to make the number of data points 2^N. Apodization of the data, i,e., appending slowly decaying tail, improves the apparent signal to noise ratio of the transform, but does not affect the frequencies and linewidths of the transform peaks. We use the power spectrum for our analysis, that is the square root of the sum of squares of sine and cosine transforms.

Thus, Fig. 2(c) shows the Fourier transform of the data of Fig. 2(a). The three strongest lines at 3.42, 5.96, and 9.38 MHz are the hyperfine splittings of the $^1D_2$ state, and their sum and harmonics give rise to the rest of the weaker lines at 6.84, 12.79, and 18.75 MHz. The apparent full width at half maximum (FWHM) of these lines is about 120 kHz, but a large part of this width is due to the finite length, 10 μsec, of the available data. Beyond 10 μsec, the photon-echo signal-to-noise ratio is small, but the modulation itself is still quite strong, indicating that the true inhomogeneous width of the hyperfine levels of $^1D_2$ should be significantly narrower. On the other hand, the high-frequency modulation due to the $^3H_4$ ground-state hyperfine structure, is quite weak and lasts less than 1 μsec, making it harder to get a good transform peak. These data are analyzed in more detail in the next section with the help of the results of the photon-echo simulation.

V. ANALYSIS

The hyperfine frequencies measured from the experiments are used to determine the hyperfine parameters P_g, P_e, η_g, and η_e. The axes orientation of the ground and the excited states is then determined by the theoretical simulation pattern that gives the best fit to the photon-echo modulation data. We now describe the details of the simulation procedure and use the results in interpreting the experimental data of the last section.

The hyperfine parameters P's and η's are determined by substituting trial values of these parameters in the ground-state and the excited-state Hamiltonians of Eq. (4). Diagonalization of the Hamiltonians gives the hyperfine splittings, which are then compared with experimental values. To proceed further, we need to express the Hamiltonians H_g and H_e of Eq. (6) in a common coordinate system, which we choose to be the (x,y,z) frame. Given a relative orientation of the two systems, the nuclear spin (I_X,I_Y,I_Z) in the excited-state coordinate system is written in terms of the same spin (I_x,I_y,I_z) in the ground-state coordinate system, using the vector transformation rule. The basis set for the Hamiltonian matrix of Eq. (6) is then

$$\{|\Psi_{\text{elec}},I_z\rangle:\ \Psi_{\text{elec}}=g,e;I_z=+\tfrac{5}{2},+\tfrac{3}{2},+\tfrac{1}{2}-\tfrac{1}{2}-\tfrac{3}{2},-\tfrac{5}{2}\}\ . \tag{17}$$

The unitary matrices U_g and U_e, and therefore the W matrix, are obtained by diagonalizing these hyperfine Hamiltonians H_g and H_e, which also yields the hyperfine frequencies $\omega^{(g)}$ and $\omega^{(e)}$. Thus we obtain all the matrices and eigenvalues needed in evaluating the photon echo amplitude of Eq. (16). Also note that in the basis system of Eq. (17), the transition dipole matrix p of Eq. (3) is a constant times identity, which is correctly implied in the derivations of Sec. II. This means that the electric dipole transition due to laser radiation cannot change the nuclear-spin state. The summation in Eq. (16) for photon echo amplitude has $6^4=1296$ terms, but there are actually only 25 distinct frequencies. (The photon echo intensity which is proportional to S^2 has 181 distinct frequencies.) Using these 25 frequencies and amplitudes the photon echo intensity is calculated as a function of the delay time τ to synthesize a photon echo modulation pattern.

As mentioned in the last section, we were unable to measure the ground-state splittings from this experiment. Instead, we use the values, 33.4, 41.6, and 75.0 MHz, reported by Shelby *et al.*[15] from optically detected NQR measurements. We have also performed several experiments[28] on the $^3P_0$-$^3H_4$ transition of the same crystal in order to find the ground-state hyperfine splittings. On this transition, we have found no modulation of the two-pulse photon echo, but the three-pulse stimulated photon echo, measured as a function of the delay time between the first two pulses, shows clear modulation pattern, and the Fourier transform of that data shows peaks at 36.0, 46.0, and 82.0 MHz. On the other hand, when we perform the PENDOR experiment by applying an rf pulse of 80 msec duration between the second and the third pulses of the stimulated photon echo, we observe 50% reduction of the echo signal at 33.6 ± 0.3 MHz, in better agreement with Shelby *et al.* We are in the process of developing a stimulated echo modulation theory, but may tentatively attribute the discrepancy to a process that enhances sum frequencies of the ground and the excited state splittings. On the other hand, it is also known that the relative sizes of the sum and difference frequency components of the PENDOR signal may be significantly affected by the delay between the first and the second pulses in the three-pulse stimulated echo sequence.[32] We confidently rule out the possibility of error in timing measurements or the Fourier transform algorithm from the fact that our experimental scheme accurately reproduces the published[10] hyperfine splittings and the photon echo modulation pattern of the $^3P_0$-$^3H_4$ transition of Pr^{3+}:LaF_3.

As for the $^1D_2$ state hyperfine splittings, our measured values, 3.42, 5.96, and 9.38 MHz, are in disagreement with Shelby *et al.*[15] using quantum-beat FID—6.49, 8.29, and 14.78 MHz. Here our justification is that we are able to reproduce the photon-echo modulation pattern quite accurately using these values, as will be shown later in this section. We have also measured the stimulated photon echo on the $^1D_2$-$^3H_4$ transition of the same crystal as a function of the time between the first two pulses. The resulting modulation pattern is essentially identical to the two-pulse echo case, and its Fourier transform shows the same three major peaks 3.4, 6.0, and 9.4 MHz, plus three more secondary peaks at 12.8, 15.4, and 18.8 MHz, which are obviously sums and harmonics of the main peaks. With the above experimental values, the best fit is found for the hyperfine parameters as

$P_g = 11.3$ MHz, $\eta_g = 0.743$ for $^3H_4$: 33.4, 41.6, and 75.0 MHz ,

$P_e = 1.52$ MHz, $\eta_e = 0.345$ for $^1D_2$: 3.42, 5.96, and 9.38 MHz .

The yttrium aluminum garnet ($Y_3Al_5O_{12}$) crystal[39–42] has overall cubic symmetry. There are eight equivalent Y^{3+} ionic sites per unit cell with site symmetry D_2, the three two-fold axes being along [100], [110], and [1$\bar{1}$0] directions. It is generally assumed that the D_2 site symmetry is preserved when an impurity ion replaces the yttrium. In such an ionic environment the principal axes system of hyperfine interaction, Eq. (4), must be parallel to the three symmetry axes. There are only six discrete possibilities of relative orientation, that is (x,y,z) parallel to (X,Y,Z) including permutations of the labels. It is surprising that none of the simulated modulation patterns using these orientations show a good match with our experimental data. The Pr^{3+} has an ionic radius of 1.013 Å and Y^{3+} 0.893 Å. If this size difference causes the Pr^{3+} ion to be shifted from the original site center along one of the symmetry axes, then the site symmetry is lowered to C_2. Then the only constraint on the relative orientation of (x,y,z) and (X,Y,Z) is that one pair of axes are parallel to each other and to the C_2 axis. There are nine possible choices of these common axes, and for each of these cases then we have one variable angle that gives the relative rotation of the two coordinate systems around the common axis.

We have done a survey where for each choice of the common axes, the relative rotation angle is varied from 0° to 90° in steps of 5°. Then the process is repeated for all nine choices of the common axes. Figure 3 shows a map of the simulated photon echo modulation patterns of such a survey. For the obvious reason of limited space we show only the cases of relative rotation angles 0° and 45° for each choice of common axes. The D_2 symmetry would restrict the map to only the six nodes, i.e., the relative rotation angle is 0°, which clearly does not match the experimental data of Fig. 2(b).

As can be seen from Fig. 3, the modulation pattern is quite a sensitive function of the axes orientation and the best fit to experimental data is found when z-axis is parallel to the X axis and the angle between the x and Y axes is 30°. Figures 2(d) and 2(e) show the plots of synthesized photon-echo modulation next to the actual experimental data. The hyperfine inhomogenous widths used in these plots are 2.2 MHz for the $^3H_4$ ground state and 20 kHz for the $^1D_2$ state. The match between the data and the simulation is quite remarkable. Figure 2(f) also shows the Fourier transform of the simulated modulation of Fig. 2(d), which matches Fig. 2(c) quite well except that the 5.96 MHz peak is smaller in the experimental data. Again, the linewidths of the simulated spectrum are limited by the finite length of the time interval of Fig. 2(d).

We have done an exhaustive survey of photon-echo modulation simulation with the various combinations of values of hyperfine splittings reported or measured, but have not found a good match between the data and the simulation, except for the above values and orientations. The explanation for the discrepancy with the previously known results probably lies in the fact that there are apparently several inequivalent sites of Pr^{3+} ions perturbed from the ideal D_2 symmetry. We have taken spectra of absorption, fluorescence excitation (total visible fluorescence versus laser wavelength), and photon echo (echo signal at fixed delay time versus laser wavelength) near 6096 Å. The absorption spectrum is essentially the same as the fluorescence excitation spectrum, which shows two peaks separated by 10 cm^{-1}, at 6092.2 and 6096.1 Å. These are the lowest two Stark levels[42,43] of $^1D_2$. In the 0.01% sample that we used for most of the experiments, the absorption is about 10% at 6092 Å and <2% at 6096 Å. On the other hand, the photon-echo spectrum is slightly more complex with at least four distinct peaks at 6091.7, 6093.6, 6096.1, and 6097.6 Å with relative sizes 2, 1, 20, and 3, respectively. The photon echo modulation

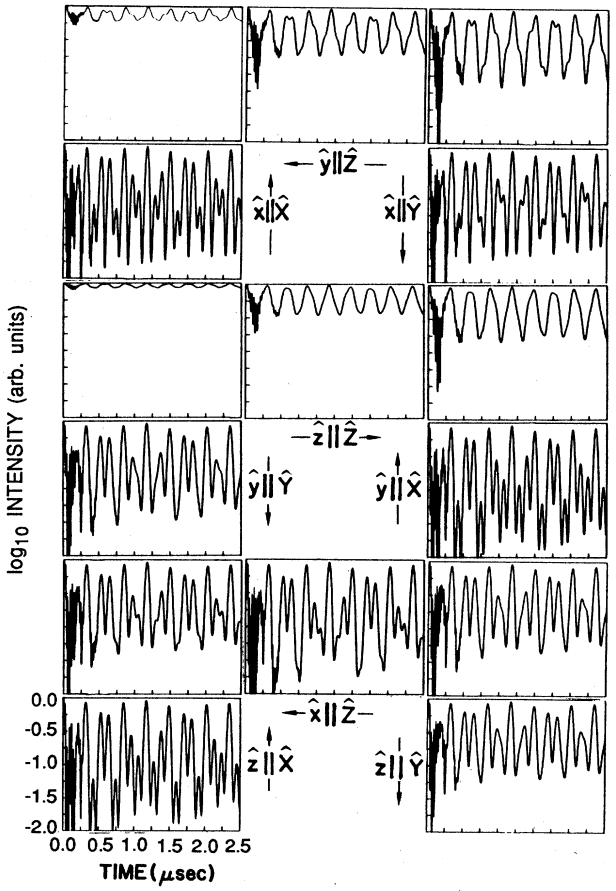

FIG. 3. Map of simulated photon-echo modulation patterns for various relative nuclear orientations. The parallel axes are indicated along with the direction of the relative angle of the other axes increases. For example, $-\hat{x}\|\hat{Y}\rightarrow$ indicates x and Y axes are parallel and $\angle(y,Z)$ increases from 0° to 90° towards the arrow.

experiments are done on the 6096-Å line. We have also measured such spectra on another 0.9% sample crystal. The overall structure of the spectra for this crystal is consistent with the 0.01% sample, except that the absorption and fluorescence excitation spectra have a few more secondary peaks, and that the photon echo is strongest at the 6098 Å line. To verify that these satellite lines are independent we also measured separate fluorescence spectrum when the laser is tuned to each of the satellite lines. The resulting spectra have similar structures with more or less proportionate shifts in line positions. The satellite lines in rare earth-doped crystals have been reported before,[40,44,45] and from the observations we made from several other crystals they seem to be quite a common occurrence. It follows that the site symmetry of the impurity ion may not necessarily be the same as that of the host ion. We conclude from the remarkable congruence of the data and the simulation in Fig. 2, that the site symmetry of the majority of Pr^{3+} ions in YAG is C_2 instead of D_2 symmetry of Y^{3+}. Polarization dependent spectral measurements are useful in determining the symmetry of atomic transitions.[45] As seen here, the photon-echo modulation is very sensitive to the symmetry of the atomic environment and should provide an additional tool for determining such symmetry.

Shelby *et al.*[15] obtained the optical homogenous width $\Gamma = 16$ kHz ($T_2 = 20$ μsec) by photon-echo decay measurement using a 0.15% sample and a single-frequency cw dye laser. Our measurements using pulsed dye lasers give $\Gamma = 61.0$ kHz ($T_2 = 5.2$ μsec). The T_2 measurements in other systems also show consistently shorter T_2 for broadband lasers than for narrowband lasers. Moreover, with narrowband lasers, the photon echo shows no hyperfine modulations. The dependence of T_2 and modulation patterns on laser linewidth is under investigation and will be discussed elsewhere.[28]

To summarize these and other results, we list in Table I the hyperfine frequencies and their inhomogenous widths of $^3P_0$, $^1D_2$ and $^3H_4$ levels of Pr^{3+} ions in both YAG and LaF_3 hosts.

TABLE I. Hyperfine splittings (ν) and their inhomogeneous widths ($\Delta\nu$, FWHM) of the $^3P_0$, $^1D_2$, and $^3H_4$ lowest Stark levels in Pr^{3+}:YAG and Pr^{3+}:LaF_3.

	Pr^{3+}:YAG		Pr^{3+}:LaF_3	
	ν (MHz)	$\Delta\nu$ (kHz)	ν (MHz)	$\Delta\nu$ (kHz)
$^3P_0$			0.73	(15)[c]
			1.12	(15)
			1.83	(25)
$^1D_2$	3.42	(20)[a]	3.72	(70)[d]
	5.96	(20)	4.79	(60)
	9.38	(20)	8.51	(30)
$^3H_4$	33.4	(300)[b]	8.48	(220)[c]
	41.6	(500)	16.68	(200)
	75.0		25.14	(240)

[a]This work.
[b]Reference 15.
[c]Reference 10.
[d]Reference 13.

VI. CONCLUSIONS

The Fourier transform of photon echo-modulation data gives hyperfine frequencies of the $^1D_2$ level of Pr^{3+}:YAG as 3.42 and 5.96 MHz. The corresponding hyperfine parameters are $P_e = 1.52$ MHz and $\eta_e = 0.345$. The photon-echo modulation pattern is a very sensitive function of these hyperfine parameters and the relative nuclear orientation of the ground and excited states. The Pr^{3+} ionic site symmetry deduced from these measurements show that the Y^{3+} ion's D_2 symmetry is lowered to C_2 when replaced by Pr^{3+} ions. These results thus demonstrate the usefulness of the photon-echo modulation technique for measurements of hyperfine parameters and for determining the symmetry of atomic environments.

ACKNOWLEDGMENTS

This research was supported by the Nippon Telegraph and Telephone Corporation. Fruitful discussions with Dr. David Huestis are gratefully acknowledged.

[1]Y. C. Chen and S. R. Hartmann, Phys. Lett. **58A**, 201 (1976).
[2]A. Z. Genack, R. M. Macfarlane, and R. G. Brewer, Phys. Rev. Lett. **37**, 1078 (1976).
[3]L. E. Erickson, Opt. Comm. **21**, 147 (1977).
[4]L. E. Erickson, Phys. Rev. B **16**, 4731 (1977).
[5]Y. C. Chen, K. P. Chiang, and S. R. Hartmann, Opt. Comm. **26**, 269 (1978).
[6]R. G. DeVoe, A. Szabo, S. C. Rand, and R. G. Brewer, Phys. Rev. Lett. **42**, 1560 (1979).
[7]Y. C. Chen, K. Chiang, and S. R. Hartmann, Opt. Comm. **29**, 181 (1979).
[8]J. B. W. Morsink and D. A. Wiersma, Chem. Phys. Lett. **65**, 105 (1979).
[9]R. M. Macfarlane, R. M. Shelby, and R. L. Shoemaker, Phys. Rev. Lett. **43**, 1726 (1979).
[10]Y. C. Chen, K. Chiang, and S. R. Hartmann, Phys. Rev. B **21**, 40 (1980).
[11]K. Chiang, E. A. Whittaker, and S. R. Hartmann, Phys. Rev. B **23**, 6142 (1981).
[12]R. M. Macfarlane and R. M. Shelby, Opt. Lett. **6**, 96 (1981).
[13]E. A. Whittaker and S. R. Hartmann, Phys. Rev. B **26**, 3617 (1982).
[14]T. Kohmoto, H. Nakatsuka, and M. Matsuoka, Jpn. J. Appl. Phys. **22**, L571 (1983).

[15]R. M. Shelby, A. C. Tropper, R. T. Harley, and R. M. Macfarlane, Opt. Lett. **8**, 304 (1983).
[16]L. Q. Lambert, Phys. Rev. B **7**, 1834 (1973).
[17]S. Meth and S. R. Hartmann, Opt. Comm. **24**, 100 (1978).
[18]M. Mitsunaga, K. Kubodera, and H. Kanbe, Opt. Lett. **11**, 339 (1986).
[19]W. B. Mims, K. Nassau, and J. D. McGee, Phys. Rev. **123**, 2059 (1961).
[20]J. A. Cowen and P. E. Kaplan, Phys. Rev. **124**, 1098 (1961).
[21]L. G. Rowan, E. L. Hahn, and W. B. Mins, Phys. Rev. **137**, A61 (1965).
[22]D. Grischkowsky and S. R. Hartmann, Phys. Rev. Lett. **20**, 41 (1968).
[23]D. Grischkowsky and S. R. Hartmann, Phys. Rev. B **2**, 60 (1970).
[24]W. B. Mims, Phys. Rev. B **3**, 2840 (1971).
[25]E. L. Hahn, Phys. Rev. **80**, 580 (1950).
[26]S. B. Grossman, A. Schenzle, and R. G. Brewer, Phys. Rev. Lett. **38**, 275 (1977).
[27]S. Haroche, J. A. Paisner, and A. L. Schawlow, Phys. Rev. Lett. **30**, 948 (1973).
[28]M. K. Kim, E. Y. Xu, and R. Kachru, (unpublished).
[29]T. W. Mossberg, R. Kachru, S. R. Hartmann, and A. M. Flusberg, Phys. Rev. A **20**, 1976 (1979).
[30]B. Bleaney, J. Appl. Phys. **34**, 1024 (1963).
[31]P. F. Liao, R. Leigh, P. Hu, and S. R. Hartmann, Phys. Lett. **41A**, 285 (1972).
[32]P. F. Liao, P. Hu, R. Leigh, and S. R. Hartmann, Phys. Rev. A **9**, 332 (1974).
[33]R. M. Shelby, R. M. Macfarlane, and R. L. Shoemaker, Phys. Rev. B **25**, 6578 (1982).
[34]L. E. Erickson, Phys. Rev. B **19**, 4412 (1979).
[35]Y. Fukuda, J. Hayashi, K. Kondo, and T. Hashi, Opt. Comm. **38**, 357 (1981).
[36]H. Harde and H. Burggraf, Opt. Comm. **40**, 441 (1982).
[37]M. Mitsunaga, E. S. Kintzer, and R. G. Brewer, Phys. Rev. Lett. **52**, 1484 (1984).
[38]L. Allen, J. H. Eberly, *Optical Resonance and Two-Level Atoms* (Wiley, New York, 1975).
[39]M. T. Hutchings and W. P. Wolf, J. Chem. Phys. **41**, 617 (1964).
[40]F. N. Hooge, J. Chem. Phys. **45**, 4504 (1966).
[41]J. T. Gourley, Phys. Rev. B **5**, 22 (1972).
[42]R. M. Macfarlane and R. M. Shelby, in *Spectroscopy of Solids Containing Rare Earth Ions,* edited by A. A. Kaplyanskii and R. M. Macfarlane (Elsevier, New York, 1987).
[43]O. L. Malta, E. Antic-Fidancev, M. Lemaitre-Blaise, Chem. Phys. Lett. **129**, 557 (1986).
[44]J. C. Vial and R. Buisson, J. Phys. (Paris) Lett. **43**, L-745 (1982).
[45]R. Bayerer, J. Heber, and D. Mateika, Z. Phys. B **64**, 201 (1986).